# Halogen Bearing Amphiboles, Aqueous Fluids, and Melts in Subduction Zones: Insights on Halogen Cycle From Electrical Conductivity

Geeth Manthilake, Kenneth T. Koga, Y. Peng, M. Mookherjee

# Halogen bearing amphiboles, aqueous fluids, and melts in subduction zones: Insights on halogen cycle from electrical conductivity

G. Manthilake[1*], K. T. Koga[1], Y. Peng[2], M. Mookherjee[2]

[1] Laboratoire Magmas et Volcans CNRS, IRD, OPGC, Université Clermont Auvergne, 63000 Clermont-Ferrand, France

[2] Earth Materials Laboratory, Department of Earth, Ocean and Atmospheric Sciences, Florida State University, Tallahassee, FL, 32306, USA

[*]Corresponding author (geeth.manthilake@uca.fr)

**Key Points:**

- The presence of F and Cl increases the electrical conductivity in aqueous fluids
- During dehydration, a fraction of F and Cl partitioned into solid phases
- F and Cl can be transported to the deep mantle by secondary minerals

**Abstract**

Amphiboles are hydrous minerals that are formed in the oceanic crust via hydrothermal alteration. The partial substitution of halogens for $OH^-$ makes amphibole one of the principal hosts of Cl and F in the subducting slab. In this study, we investigated the electrical conductivity of a suite of halogen bearing amphibole minerals at 1.5 GPa up to 1400 K. The discontinuous electrical behavior indicate dehydration of amphibole at ~915 K. This is followed by dehydration induced hydrous melting at temperatures above 1070 K. We find that the released aqueous fluids have an electrical conductivity of ~0.1 S/m. This high electrical conductivity is likely to explain anomalously high electrical conductivity observed in certain subduction zone settings. This high electrical conductivity of an order of magnitude greater than the electrical conductivity of pure aqueous fluids at similar conditions is likely due to the partitioning of the F and Cl into the aqueous fluids. We also noted that subsequent to the dehydration, secondary phases form due to the breakdown of the primary halogen bearing amphibole. Chemical analyses of these secondary phases indicate that they are repositories of F and Cl. Hence, we infer that upon dehydration of the primary halogen bearing amphibole, first the F and Cl are partitioned into the aqueous fluids and then the halogens are partitioned back to the secondary mineral phases. These secondary minerals are likely to transport the halogen to the deep Earth and may in part explain the halogen concentration observed in ocean island basalt.

## Plain language summary

Amphiboles are one of the principal mineral phases that accommodate halogens in the subducting slab. The aqueous fluid released during the dehydration of amphibole dissolves and transfers halogens into the overlying wedge mantle. The resulting fluid exhibits high electrical conductivity. Our study also indicates that a significant portion of F and small quantities of Cl carried by amphibole are partitioned back to the secondary mineral phases that result from the breakdown of the primary amphibole. These secondary mineral phases are likely to transport halogen into the Earth's interior and may explain the distinct halogen contents observed between lower mantle-derived ocean island basalts compared to MORB sources.

## 1. Introduction

Amphiboles are hydrous minerals present in the altered oceanic crust and play a vital role in transporting hydrophile elements including halogen into the deep mantle via subduction of oceanic plates (Debret et al., 2016; Ito et al., 1983). The crystal structure of amphibole consists of corner-sharing tetrahedral units linked to form double chains and edge-sharing octahedral units. The octahedral strip is sandwiched between two tetrahedral double chains with their apices pointing towards each other forming an I-beam. These minerals also contain ~ 2 wt % water crystallographically bound as hydroxyl ($OH^-$) units. The interaction of saline seawater with oceanic crust often helps to incorporate Cl and F into the amphibole crystal structure. These halogen ions, $Cl^-$ and $F^-$ readily substitutes for the hydroxyl ($OH^-$) units (Kendrick et al., 2011). As the subducting slabs experience higher temperatures at depths, hydrous minerals including amphibole dehydrate. And upon dehydration, Cl and F in the amphibole crystal structure are likely to partition into the released aqueous fluid. However, based on experimental results it seems that Cl is likely to partition into aqueous fluid far more easily than F (Bernini

et al., 2013; Fabbrizio et al., 2013a; Fabbrizio et al., 2013b). When amphibole or apatite is present with an aqueous fluid, F partitions into these minerals instead of fluid (Brenan, 1993; Wu & Koga, 2013, 2018). During partial melting, these elements are incompatible with minerals (Beyer et al., 2012, 2016; Dalou et al., 2012, 2014). However, highly incompatible Cl may readily partition into the melt phase while moderately incompatible F may incorporate into minerals with hydroxyl-sites (Van den Bleeken & Koga, 2015; Mathez & Webster, 2005; Webster et al., 2009).

Magnetotelluric (MT) studies provide crucial information on the presence of aqueous fluids and/or melts in Earth's interior. Interpretation of MT results based on the laboratory-based electrical conductivity of minerals, fluids, and melts has been fundamental in the characterization of the degree of mantle hydration (Freitas & Manthilake, 2019; Soyer & Unsworth, 2006), circulation of aqueous fluids in the upper mantle (Manthilake et al., 2015; Manthilake et al., 2016), and melting (McGary et al., 2014; Zhang et al., 2014). A few studies have discussed the electrical conductivity of fluids bearing systems (Guo & Keppler, 2019; Guo et al., 2015; Reynard et al., 2011; Sakuma & Ichiki, 2016; Shimojuku et al., 2012, 2014; Sinmyo & Keppler, 2017). These studies have characterized saline fluid compositions that are appropriate for shallow crustal fluids. However, the fluids released in subduction zones and at conditions relevant for deeper mantle are likely to be different from such crustal fluids. At greater depths, aqueous fluids often evolve to supercritical fluids and may have enhanced electrical conductivities (Manthilake et al., 2015; Mitchell & Nellis, 1982). In addition, the effect of halogen on aqueous fluids under these conditions remains unknown.

The thermodynamic stability of amphibole in subducting slabs is often dictated by the composition. For instance, the hydrous amphibole phase is likely to break down at around ~80 km depth (Schmidt & Poli, 1998). In contrast, the thermal stability of $F^-$ and/or $Cl^-$ bearing amphibole is greater and may be stable beyond depths of 80 km (Foley, 1991; Holloway &

96 Ford, 1975). A related key question is, when halogen bearing amphiboles dehydrate, do all the
97 halogens partition to the aqueous fluids and eventually recycled back to the Earth's surface? Or
98 is there a fraction of halogens sequestered into nominally anhydrous phases and are transported
99 into the deep Earth?

100 The relatively stable halogen levels in world oceans suggest that the amount of halogen
101 entering into the Earth's interior via subduction would go through efficient recycling processes
102 and re-emitted at the arc volcanoes (Wallace, 2005). While most of the halogens are recycled
103 at shallower depths (Scambelluri et al., 2004), the recent reports of higher concentrations of Cl
104 and F in the lower mantle-derived oceanic island basalts magmas (OIB) indicate a possibility
105 of subducting halogens into the Earth's lower mantle (Hanyu et al., 2019; Jackson et al., 2015;
106 Kovalenko et al., 2006; Rose-Koga et al., 2017). These recent reports have also prompted
107 experimental studies on the solubility of halogen in mineral phases of the transition zone and
108 lower mantle (Roberge et al., 2017; Yoshino & Jaseem, 2018) which also suggests that these
109 deep mantle phases could sequester halogens to the deep Earth.

110 Hence, in order to understand the fate of halogens during the dehydration of halogen
111 bearing amphibole at subduction zone conditions, in this study, we investigate the electrical
112 conductivity of four chemically distinct, Cl, and F bearing amphibole compositions at 1.5 GPa
113 up to 1400 K. We characterize the electrical conductivity of the aqueous fluid and if halogens
114 are partitioned into the fluids, does that affect the electrical conductivity and we compare
115 laboratory data with MT data to better understand subduction settings where these results are
116 applicable. Also, we characterize the secondary mineral phases to evaluate whether all the
117 halogens are lost to the aqueous fluids or are there a fraction of halogen sequestered into
118 secondary phases which may transfer it to deep Earth and explain the halogen concentrations
119 observed in OIB.

## 2. Methods

For the electrical conductivity experiments, four natural amphibole samples, ferri-kaersutite (Dontresse, Cézalier, France), actinolite (Russel, NY, USA), hastingsite (Lenzo, Italy), and tremolite (Russel, NY, USA) were used. These four distinct samples have varying concentrations of halogens i.e., Cl and F. The chemical composition of amphiboles was analyzed using a Cameca SxFiveTactis electron microprobe. The electron probe microanalysis was conducted with an accelerating voltage of 15 kV and a beam current of 20 nA. F and Cl were measured by electron microprobe using three Fe interference-free Thallium acid phthalate (TAP) crystals (Rose-Koga et al., 2020). The concentrations of F and Cl in the four natural amphibole samples were also determined using an IMS 1270 secondary-ion mass spectrometer (SIMS) at Centre de Recherches Pétrographiques et Géochimiques (CRPG) Nancy, France.

To prepare the samples for the electrical conductivity measurements, first, the large crystals of natural amphibole were broken down to smaller sized crystals. Then, the inclusion-free smaller sized crystals were handpicked under the binocular microscope. These smaller inclusion-free crystals were then crushed into finely powdered samples. These powdered samples were placed in cylindrical rhenium (Re) capsule and hot-pressed at 1.5 GPa and 700 K for 1 hour. Hot pressing of the sample and electrical conductivity experiments at high pressures and temperatures were performed using a 1500-ton multi-anvil apparatus installed at the Laboratoire Magmas et Volcans. The electrical conductivity measurements were performed in 18/11 multi-anvil assemblies i.e., 18 mm edge length of the MgO octahedral pressure medium and 11 mm of the truncated edge length of the first stage anvils made up of tungsten carbide (WC) (**Fig. 1a**). Pre-sintered cylindrical samples were placed in a polycrystalline hBN capsule. The high purity hBN, sintered at higher temperature and pressure without boron (B) binder (BNHP- FINAL Advanced Materials, France) ensured that there were no $B_2O_3$ forming

reactions with the aqueous fluids. The fine grain size of the sintered hBN also reduced the possibility of fluid escape from the sample at high temperatures. Nickel (Ni) disks were placed at the opposite ends of the cylindrical sample. These Ni disks were used as electrodes for the electrical conductivity measurements. These Ni disks also served to regulate the oxygen fugacity ($f_{O_2}$) Ni-NiO which is similar to the Fayalite-Magnetite-Quartz (FMQ) buffer (Frost, 1991). The temperature of the sample was monitored with a $W_{95}Re_5$-$W_{74}Re_{26}$ thermocouple junction placed at one side of the sample. Sample resistance was obtained using the leads from the thermocouple and a separate $W_{95}Re_5$ cable placed at the opposite side of the sample. MgO ceramic sleeves were placed to insulate the electrode wires from the furnace. To avoid the exposure of assembly components to atmospheric moisture and other impurities, ceramic assembly parts were baked at 1273 K and stored at 400 K in high- vacuum furnaces prior to assembling.

Electrical resistivity was determined using the impedance spectroscopy method in the frequency range of $10^6$-$10^1$ Hz. At the desired pressure, samples were kept at 500 K for several hours to remove the absorbed moisture in the sample capsule and the surrounding area, which improves the insulation resistance of the assembly (Manthilake et al., 2015). The sample resistance was measured at temperature steps of 50-100 K with increasing temperature beyond the thermodynamic stability of amphiboles. We have also collected data along the cooling cycle. along with the heating and cooling cycle. The resistance of polycrystalline samples can be modeled by a combination of resistor-capacitor (R-C) or resistor-constant phase element (R-CPE) circuits (**Fig. 2**). The electrical conductivity of the polycrystalline sample can be determined by the resistance from impedance spectra, and the dimension of the sample i.e., diameter and length, measured after each experiment (**Fig. 1b-e**).

The dependence of the electrical conductivity of the polycrystalline sample with inverse temperature exhibits Arrhenius relation (**Fig.3**). The activation enthalpy ($\Delta H$) of the conduction

mechanisms operating at different temperature intervals can be determined according to the Arrhenius equation, $\sigma = \sigma_0 exp(-\Delta H|RT)$, where $\sigma$ is the electrical conductivity (S/m), $T$ is the absolute temperature, $\sigma_0$ is the pre-exponential factor (S/m), and $R$ is the universal gas constant (J/K.mol).

In addition to the chemical compositions of the natural amphiboles used for the electrical conductivity studies, the chemistry and the modal abundances of the secondary phases, following the *in-situ* electrical conductivity experiments, were also investigated using the Cameca SxFiveTactis electron microprobe. Unreacted primary minerals and secondary mineral assemblages from the breakdown of the primary amphiboles due to dehydration were characterized using energy-dispersive x-ray spectroscopy (EDS) chemical mapping. The composition of the fluid and the melt phases were determined by mass-balance calculations based on the mineral proportions and their chemical compositions of recovered samples following the dehydration and dehydration-induced partial melting (Locock, 2014).

## 3. Results

The discontinuous increase of electrical conductivity with increasing temperature was observed in all experimental runs (**Fig. 3**). We note that heating of the sample above the pre-sintering temperature does not significantly enhance the electrical conductivity. However, we have observed a reduction of the noise in the impedance spectra during the high T annealing. This is likely due to the healing of microcracks developed during the compression. The discontinuous trends can be used to determine the changes that the sample undergoes including dehydration and dehydration-induced melting (Freitas and Manthilake, 2019; Manthilake et al., 2015; Manthilake et al., 2016). The electrical conductivity of amphibole was characterized by two main conductivity discontinuities, the first discontinuity occur over a temperature range of 915-933 K and the second discontinuity is often observed over a temperature range of 1070-

1170 K. These observed discontinuities in electrical conductivity vs. inverse temperature can be separated into three distinct temperature intervals: at temperatures lower than 900 K, the electrical conductivity is dominated by the polycrystalline mineral sample, between 900 and 1100 K, the electrical conductivity is due to aqueous fluids released by dehydration of amphibole, and at temperatures greater than 1100 K, the electrical conductivity is due to the dehydration-induced hydrous silicate melt (**Fig. 3**). The dehydration temperatures observed for a suite of amphiboles that are likely to be stable in different lithologies in the Earth's mantle ranges between 1200 to 1300 K (Mandler & Grove, 2016). We note the enhancement in the electrical conductivity is in good agreement with the dehydration-induced melting observed in amphibolites (Wyllie & Wolf, 1993). The electrical conductivities of dehydrating fluids were similar with little or no variations (~0.1 S/m) across all starting compositions. The electrical conductivity of the hydrous melt produced by the melting of ferri-kaersutite, actinolite, hastingsite 6, 8, and 8 S/m respectively, at the highest temperature measured in each heating cycles, while tremolite exhibited slightly lower conductivity of about 2 S/m at 1403 K.

The increase of electrical conductivity with increasing temperature after the dehydration and subsequent dehydration-induced melting of amphibole is likely to be related to (a) the interconnectivity of the liquid phase governed by their ability to wet the grain boundaries, and (b) the increase of fluid/melt fraction in the samples as observed in prior studies on different samples (Freitas et al., 2019). It is known that the dihedral angle of aqueous fluids decreases with increasing pressures and temperatures (Manthilake et al., 2015; Mibe et al., 1999; Yoshino et al., 2002). This points toward the enhancement of grain boundary wetting by aqueous fluid in subduction zones. In partially molten samples, the dihedral angle decreases at high pressures and enhanced water contents (Freitas et al., 2017; Yoshino et al., 2009). The high water contents observed in our melt suggests that hydrous silicate melt produced by the released aqueous fluids from dehydration of amphiboles are efficient in wetting the grain boundaries. The experimental

conditions explored in our experiments are likely to produce aqueous fluids and melt dihedral angles that result in excellent inter-connectivity of fluid/melt phase which in turn helps in enhanced electrical conductivity even at lower fluid/melt fractions.

We confirmed the partial breakdown of amphibole with detailed electron microprobe analysis, scanning electron microscopy images, and energy-dispersive X-ray spectroscopy (EDS) elemental mapping of recovered samples (**Fig. 4)**. The experimental run products indicate dehydration and breakdown of amphibole to secondary mineral phases (**Table 1**). For instance in the experiments (#555), upon dehydration, actinolite completely transforms into a mixture of clinopyroxene (cpx) and orthopyroxene (opx). The orthopyroxene (opx) inherited an amphibole-like elongated form (**Fig. 4b**). In additional experiments (#554, 567, 576), upon dehydration, Fe-kaersutite (#554), hastingsite (#567), and tremolite (#576), transforms to an assemblage consisting of cpx, opx, gt, and secondary amphiboles (**Fig. 4a,c,d**). In addition, we also find relics of pristine or primary amphibole. Relics of pristine amphiboles are often recognizable with SEM images (**Fig. 4**). In all experiments, the dehydration-induced fluids triggered partial melting and crystallized a suite of secondary amphiboles upon a gradual decrease in temperature. The secondary amphiboles showed strong F enrichment and moderate Cl contents compared to the melt phase (**Fig. 5**)

## 4. Discussion

### 4.1. Electrical conductivity of the halogen-bearing dehydrating fluid

We observed that the electrical conductivity of halogen bearing fluids is more than a factor of ten or higher compared to the halogen-free aqueous fluids reported in earlier studies (Guo et al., 2011; Manthilake et al., 2016; Wang and Karato, 2013) **(Fig. 6)**. Based on the partitioning behavior, it is generally assumed that upon dehydration, $F^-$ and $Cl^-$ ions in amphibole are readily partitioned into the aqueous fluid phase, making dehydrating fluids in

the mantle wedge rich in F and Cl. Because of their highly ionic nature, the aqueous fluids containing halogens are good electrical conductors (Guo & Keppler, 2019; Reynard et al., 2011; Shimojuku et al., 2012, 2014; Sinmyo & Keppler, 2017).

Partitioning of halogen between aqueous fluids and anhydrous minerals including olivine and pyroxenes show that Cl and F are dominantly incorporated into the fluid phase (Bernini et al., 2013; Fabbrizio et al., 2013a; Fabbrizio et al., 2013b). However, the chemical analyses of our experimental run products after partial dehydration of amphibole suggest that F and Cl are mostly partitioned into the secondary mineral phases such as edenite and garnet, (**Table 2**). It has been shown that the halogen concentrations in secondary amphiboles in equilibrium with the fluid are lower than the primary amphiboles. (Bernini et al., 2013; Wu & Koga, 2013, 2018). The increase of electrical conductivity of the fluid phase compared to halogen-free fluids can be attributed to the fraction of F and Cl dissolved in the fluid.

### 4.2 Electrical conductivity of hydrous melt

The dehydration-induced hydrous silicate melts produced by ferri-kaersutite, actinolite, hastingsite, and tremolite amphibole compositions, all have electrical conductivities within the range 2-8 S/m. (**Fig. 3**). The electrical conductivity of melt produced by the melting of amphibole in the slab closely resembles the values obtained for basalts commonly found in volcanic-arc settings (Gailler et al., 2019) (**Fig. 6**). This demonstrates that distinguishing the precursor compositions of most hydrous melts based on the electrical conductivity is often challenging and hint towards the broad similarities in electrical charge carrier concentrations in both types of melts.

The diverse chemical composition of amphiboles used in this study enables us to investigate the efficiency of charge-carrying cations in hydrous silicate melts (**Fig. 7**). We observe that the increase in the concentrations of $Na^{+}$ and $Fe^{2+}/Fe^{3+}$ show strong positive

correlation with the electrical conductivity of the melt (**Fig. 7 a,b**). However, we find that an increase in the $Ca^{2+}$ ion concentrations has an inverse effect on electrical conductivity in the melt (**Fig. 7c**). It has been shown that the electrical conductivity and the diffusivity in silicate melts strongly depended on the degree of polymerization (Mills, 1993). The increase of network-breaking $Ca^{2+}$ results in breaking of bonding-oxygen in $SiO_4^{4-}$ tetrahedral and bind with non-bridging oxygen forming both polymerized and depolymerized units (Lee & Stebbins, 2006; Maroufi et al., 2016; Mills, 1993). An increase of CaO concentrations affects the number of such anionic units present in the melt (Mills, 1993). The negative correlation observed between the electrical conductivity and the concentration of CaO, could be attributed to the increase of polymerized anions in the melt.

### 4.3 Implications for the wedge-mantle electrical anomalies

The observed electrical conductivity anomalies in subduction zone settings are often linked with the presence of aqueous fluids (McGary et al., 2014). Support for this argument is further reinforced by numerous electrical conductivity studies based on laboratory experiments which demonstrate higher electrical conductivities for aqueous fluid compared to solid mineral phases (Manthilake et al., 2015; Manthilake et al., 2016; Manthilake et al., 2021a; Reynard et al., 2011; Shen et al., 2020; Wang et al., 2012; Wang and Karato, 2013; Zhang et al., 2014). Upon dehydration, the released fluids may lead to the formation of an interconnected network of a conductive phase (fluid/ melt). This interconnected network of highly conductive fluid/melt could dominate the bulk conductivity of rock and mask the relatively resistive matrix made up of remaining mineral phases. Similarly, an interconnected network of fluids/melt also affects the shear modulus of the rock, reducing both compressional and shear wave velocities (Chantel et al., 2016; Freitas et al., 2017, 2019; Manthilake et al., 2021b; Soustelle et al., 2014;Weidner et al., 2018). The concomitant reduction of seismic wave velocities and the seismic attenuation

295 is considered as a strong indication of the presence of a liquid phase. However, given that high
296 electrical conductivities could also be caused by thin films of graphite (Glover, 1996) or
297 crystalline precipitates of metal oxides (Manthilake et al., 2016), a cross-correlation between
298 seismic and electrical signatures are often warranted (Freitas et al., 2019).

299 Several subduction zone settings exhibit elevated electrical conductivity at depths of 40
300 and 100 km in the wedge mantle. Moderate to high electrical conductivity anomalies have been
301 observed in the Cascadia subduction system (CSZ) (Evans et al., 2014; McGary et al., 2014),
302 Cocos subduction system in Sothern Mexico (SM) (Jödicke et al., 2006), Marlborough, New
303 Zealand (NZ) (Wannamaker et al., 2009) Northwestern Costa Rica (CR) (Brasse et al., 2009;
304 Worzewski et al., 2011), Bolivia-Altiplano (BVA) (Brasse et al., 2002), Bolivian Orocline
305 (BVO) (Brasse & Eydam, 2008) and Southern Kyushu (KYU) (Ichiki et al., 2000). These
306 observations of elevated electrical conductivity can often be explained by the presence of
307 aqueous fluid released by dehydration. The depth-dependent MT data from these subduction
308 systems show three clusters of electrical conductivities (**Fig. 8**). Several locations including
309 Northwestern Costa Rica (CR), Sothern Mexico (SM), Marlborough, New Zealand(NZ),
310 Cascadia-Mount Rainier (CAS-MR) (McGary et al., 2014), Sothern Kyushu (Ichiki et al., 2000)
311 exhibits electrical conductivity ~0.1 S/m. The second cluster of electrical conductivity~ 1 S/m
312 is shown by subduction zones including Cascadia-Oregon (CAS-OR) (Evans et al., 2014),
313 Bolivia-Altiplano (BVA) (Brasse et al., 2002). The third cluster of electrical conductivity ~ 1
314 S/m is observed at greater depths 50-100 km, these include Bolivia-Altiplano (BVA) (Brasse
315 et al., 2002), Bolivian Orocline (BVO) (Brasse & Eydam, 2008). The clear distinction between
316 these two shallow clusters could be due to variation in thermal state of the subduction zone, the
317 physical state of the conductive phase, i.e., aqueous fluid, melt/super critical fluids, or
318 conductive solid, and the chemical composition of the conducive phase.

Could the observed variation of electrical conductivity between these two states be attributed to the salinity of the aqueous fluids? It is well known that electrical conductivity of ~0.1 S/m can be explained by 30 ‰ salinity in aqueous fluids (Manthilake et al., 2016; Shimojuku et al., 2012, 2014; Sinmyo and Keppler, 2017). 30 ‰ salinity is close to the salinity expected at natural seawater. However, electrical conductivity observed for the second cluster i.e., ~1 S/m requires fluid with extremely high salinities of more than 100 ‰ (Manthilake et al., 2016). Our study indicates that the high salinities of ~ 100 ‰ may not be achieved in naturally occurring fluids in subduction zones as halogen partitions into thermodynamically stable secondary mineral phases in the downgoing slab (**Table 2**). Naturally occurring fluid inclusions from subduction-related orogenic ophiolites could have salinities up to ~89 ‰ salinity (Kawamoto et al., 2018). But this high salinity is rare and only occurs in extreme cases, the average salinity is ~45 ‰ (Kawamoto et al., 2018). The expected salinity of our experimental charge, calculated based on the Cl and F partitioned into the fluid phase, is 24 ‰ for Fe kaersutite, 27 ‰ hastingsite, 12 ‰ tremolite, and 0.03 ‰ actinolite. We conclude that the high conductivity anomalies around 0.1 S/m are the range that can be explained by dehydrating fluids exiting from the slab, which contain halogens.

The high conductivity anomalies of more than 1 S/m found in subduction systems are located at two distinctive regions relative to the slab (Brasse et al., 2002; Evans et al., 2014; Soyer & Unsworth, 2006). The first location is found at the nose of the mantle wedge in the depth range 20-40 km and shown to have a much smaller spatial distribution (Brasse et al., 2002; Evans et al., 2014; Jödicke et al., 2006; Wannamaker et al., 2009). The second anomaly is located at 60-120 km depths beneath the arc and shows the larger spatial distribution (Brasse et al., 2002; Brasse & Eydam, 2008; Evans et al., 2014; McGary et al., 2014). The anomaly found at the nose of the wedge has been explained by solid conductors such as interconnected magnetite along grain boundaries, which can be precipitated during the dehydration of chlorite

(Manthilake et al., 2016). When the electrical anomalies are associated with negative seismic anomalies, such as those found at 60-120 km beneath the arc, an inter-connected liquid must be present in the region. Because the saline fluid in the natural arc setting is not expected to increase the conductivity to 1 S/m, we conclude that a hydrous silicate melt is the likely cause of high conductivity observed at the depth range 60-120 km (**Fig. 8**). If an anomaly is located within the mantle wedge, the partial hydrous silicate melt is likely to be feeding the arc magmatism. If the anomaly is situated near the slab-mantle wedge interface, the partial melt is expected to be that of slab-derived melt, such as partial melting of sediments and/or mafic crust. In either case, small degrees of the partial melt is high in volatile and incompatible elements such as $H_2O$ and Na, and such compositional tendency is consistent with high conductivity (**Fig. 8**).

### 4.4 Implications for the transport of halogen into the deep mantle

Recycling of halogen in the subduction zone settings is directly tied to the aqueous fluids/melts released from the subducting slab. The aqueous fluid is an efficient carrier of easily ionizing halogens, except for F in certain circumstances. Based on the balance of the subduction input and the output from arc volcanoes, nearly all of Cl is recycled back to the surface. In contrast to Cl, more than 90 % of F is estimated to be partitioned to either reservoir located at the wedge mantle or, to deep mantle reservoirs (Straub & Layne, 2003). Experimentally determined partition coefficients also indicate that F is likely to be partitioned to the residual amphibole during dehydration-induced melting (Wu & Koga, 2013).

However, both Cl and F can be partitioned to hydrous silicate melts and be effectively removed from the slab, thus increasing F and Cl contents in arc magma (Van den Bleeken and Koga, 2015; Beyer et al. 2016). However, even in the presence of hydrous silicate melt, F is moderately incompatible and can in sequestered in the crystalline structure of minerals

including amphibole, mica, and apatite. Thus, some amount of F is expected to be transported into the deep mantle via secondary mineral phases (**Fig. 5**). Because of the distinct partitioning behavior of halogen (F) in melt and aqueous fluids, the efficiency of the halogen recycling is likely to be controlled by the nature of the fluid phase in the subducting slab. This might be further complicated by the presence of supercritical fluids which could enhance the partitioning of elements into the fluids (Kessel et al., 2005). Thus, the injection of halogen into the deep mantle varies greatly from one arc to another depending on the type of liquid coming out of the slab (fluid or slab melt). Our study provided a crucial link between the halogen induced enhanced electrical conductivity of aqueous fluids and melts and also the partitioning of halogen in secondary phases such as amphibole and garnet that could sequester halogens such as F and Cl and transfer them to the deep Earth. Once halogen is subducted into the transition zone and lower mantle, the high-pressure phases can accommodate these elements in its crystalline structure and it is not expected to produce significant fractionation during the mantle convection.

Variable degrees of halogen recycling has already been inferred based on the distribution of halogens in ocean island basalts. Much of the variations of Cl and F abundances are often attributed to near-surface contamination (Kendrick et al., 2015). However, there are variations in the concentration of halogens that could be attributed to the variations related to the source of the OIBs (Kovalenko et al., 2006; Jackson et al., 2015; Rose-Koga et al., 2017; Hanyu et al., 2019; Kendrick et al. 2015). An increase of F in ocean island basalts compared to a MORB source mantle appears to correlate with the radiogenic Pb signature establishing the direct relationship between recycling slab and F enrichment (Rose-Koga et al., 2017).

**Acknowledgments**

We thank J-M Henot (deceased) and E. Voyer for help with the SEM analyses, J-L Davidal for the electron microprobe analyses, and Antoine Mathieu for the technical assistance. Christian Nicollet is thanked for providing some natural amphiboles. GM acknowledges funding from the INSU-CNRS. M.M. is supported by the US National Science Foundation grants, EAR 1753125, 1763215. This research was financed by the French Government Laboratory of Excellence initiative n°ANR-10-LABX-0006, the Région Auvergne, and the European Regional Development Fund (ClerVolc contribution number 454). The authors comply with AGU's data policy, and the data of this study are available in Zonodo (http://doi.org/10.5281/zenodo.4267663). The authors declare no competing financial interests.

**References**

Bernini, D., Wiedenbeck, M., Dolejš, D., & Keppler, H. (2013). Partitioning of halogens between mantle minerals and aqueous fluids: Implications for the fluid flow regime in subduction zones. *Contributions to Mineralogy and Petrology*, *165*(1), 117–128. https://doi.org/10.1007/s00410-012-0799-4

Beyer, C., Klemme, S., Wiedenbeck, M., Stracke, A., & Vollmer, C. (2012). Fluorine in nominally fluorine-free mantle minerals: Experimental partitioning of F between olivine, orthopyroxene and silicate melts with implications for magmatic processes. *Earth and Planetary Science Letters*, *337–338*, 1–9. https://doi.org/10.1016/j.epsl.2012.05.003

Beyer, C., Klemme, S., Grützner, T., Ireland, T. R., Magee, C. W., & Frost, D. J. (2016). Fluorine partitioning between eclogitic garnet, clinopyroxene, and melt at upper mantle conditions. *Chemical Geology*, *437*, 88–97. https://doi.org/10.1016/j.chemgeo.2016.05.032

Van den Bleeken, G., & Koga, K. T. (2015). Experimentally determined distribution of fluorine and chlorine upon hydrous slab melting, and implications for F-Cl cycling through subduction zones. *Geochimica et Cosmochimica Acta*, *171*, 353–373. https://doi.org/10.1016/j.gca.2015.09.030

Brasse, H., & Eydam, D. (2008). Electrical conductivity beneath the Bolivian Orocline and its relation to subduction processes at the South American continental margin. *Journal of Geophysical Research: Solid Earth*, *113*(7), 1–14. https://doi.org/10.1029/2007JB005142

Brasse, H., Lezaeta, P., Rath, V., Schwalenberg, K., Soyer, W., & Haak, V. (2002). The Bolivian Altiplano conductivity anomaly. *Journal of Geophysical Research-Solid Earth*, *107*(B5), 17. https://doi.org/2096 Artn 2096

Brasse, H., Kapinos, G., Mütschard, L., Alvarado, G. E., Worzewski, T., & Jegen, M. (2009). Deep electrical resistivity structure of northwestern Costa Rica. *Geophysical Research Letters*, *36*(2), 1–5. https://doi.org/10.1029/2008GL036397

Brenan, J. M. (1993). Diffusion of chlorine in fluid-bearing quartzite: effects of fluid composition and total porosity. *Contributions to Mineralogy and Petrology*, *115*(2), 215–224. https://doi.org/10.1007/BF00321221

Chantel, J., Manthilake, G., Andrault, D., Novella, D., Yu, T., & Wang, Y. (2016). Experimental evidence supports mantle partial melting in the asthenosphere. *Science Advances*, *2*(5), e1600246. https://doi.org/10.1126/sciadv.1600246

Dalou, C., Koga, K. T., Shimizu, N., Boulon, J., & Devidal, J. L. (2012). Experimental determination of F and Cl partitioning between lherzolite and basaltic melt. *Contributions to Mineralogy and Petrology*, *163*(4), 591–609. https://doi.org/10.1007/s00410-011-0688-2

Dalou, C., Koga, K. T., Le Voyer, M., & Shimizu, N. (2014). Contrasting partition behavior

of F and Cl during hydrous mantle melting: implications for Cl/F signature in arc magmas. *Progress in Earth and Planetary Science*, *1*(1), 1–17. https://doi.org/10.1186/s40645-014-0026-1

Debret, B., Koga, K. T., Cattani, F., Nicollet, C., Van den Bleeken, G., & Schwartz, S. (2016). Volatile (Li, B, F and Cl) mobility during amphibole breakdown in subduction zones. *Lithos*, *244*, 165–181. https://doi.org/10.1016/j.lithos.2015.12.004

Evans, R. L., Wannamaker, P. E., McGary, R. S., & Elsenbeck, J. (2014). Electrical structure of the central Cascadia subduction zone: The EMSLAB Lincoln Line revisited. *Earth and Planetary Science Letters*, *402*(C), 265–274. https://doi.org/10.1016/j.epsl.2013.04.021

Fabbrizio, A., Stalder, R., Hametner, K., & Günther, D. (2013). Experimental chlorine partitioning between forsterite, enstatite and aqueous fluid at upper mantle conditions. *Geochimica et Cosmochimica Acta*, *121*, 684–700. https://doi.org/10.1016/j.gca.2013.05.026

Fabbrizio, A., Stalder, R., Hametner, K., Günther, D., & Marquardt, K. (2013). Experimental partitioning of halogens and other trace elements between olivine, pyroxenes, amphibole and aqueous fluid at 2 GPa and 900-1,300 °C. *Contributions to Mineralogy and Petrology*, *166*(2), 639–653. https://doi.org/10.1007/s00410-013-0902-5

Foley, S. (1991). High-pressure stability of the fluor- and hydroxy-endmembers of pargasite and K-richterite. *Geochimica et Cosmochimica Acta*, *55*(9), 2689–2694. https://doi.org/10.1016/0016-7037(91)90386-J

Freitas, D., & Manthilake, G. (2019). Electrical conductivity of hydrous silicate melts : Implications for the bottom-up hydration of Earth ' s upper mantle. *Earth and Planetary Science Letters*, *523*, 115712. https://doi.org/10.1016/j.epsl.2019.115712

Freitas, D., Manthilake, G., Schiavi, F., Chantel, J., Bolfan-Casanova, N., Bouhifd, M. A., &

Andrault, D. (2017). Experimental evidence supporting a global melt layer at the base of the Earth's upper mantle. *Nature Communications*, *8*(1), 2186. https://doi.org/10.1038/s41467-017-02275-9

Freitas, D., Manthilake, G., Chantel, J., Bouhifd, M. A., & Andrault, D. (2019). Simultaneous measurements of electrical conductivity and seismic wave velocity of partially molten geological materials: effect of evolving melt texture. *Physics and Chemistry of Minerals*, *46*(6), 535–551. https://doi.org/10.1007/s00269-019-01021-5

Frost, B. R. (1991). Introduction to oxygen fugacity and its petrologic importance. In D. . Lindsley (Ed.), *Reviews in Mineralogy: Oxide Minerals: Petrologic and Magnetic Significance* (pp. 1–9).

Gailler, L., Kauahikaua, J., Lénat, J. J.-F., Revil, A., Gresse, M., Ahmed, A. S., et al. (2019). 3D electrical conductivity imaging of Halema'uma'u lava lake (Kīlauea volcano). *Journal of Volcanology and Geothermal Research*. https://doi.org/10.1016/j.jvolgeores.2019.06.001

Guo, H., & Keppler, H. (2019). Electrical Conductivity of NaCl-Bearing Aqueous Fluids to 900 °C and 5 GPa. *Journal of Geophysical Research: Solid Earth*, *124*(2), 1397–1411. https://doi.org/10.1029/2018JB016658

Guo, X., Yoshino, T., & Katayama, I. (2011). Electrical conductivity anisotropy of deformed talc rocks and serpentinites at 3GPa. *Physics of the Earth and Planetary Interiors*, *188*(1–2), 69–81. https://doi.org/10.1016/j.pepi.2011.06.012

Guo, X., Yoshino, T., & Shimojuku, A. (2015). Electrical conductivity of albite-(quartz)-water and albite-water-NaCl systems and its implication to the high conductivity anomalies in the continental crust. *Earth and Planetary Science Letters*, *412*, 1–9. https://doi.org/10.1016/j.epsl.2014.12.021

Hanyu, T., Shimizu, K., Ushikubo, T., Kimura, J. I., Chang, Q., Hamada, M., et al. (2019).

492 Tiny droplets of ocean island basalts unveil Earth's deep chlorine cycle. *Nature*
493 *Communications*, *10*(60), 1–7. https://doi.org/10.1038/s41467-018-07955-8
494 Holloway, J. R., & Ford, C. E. (1975). Fluid-absent melting of the fluoro-hydroxy amphibole
495 pargasite to 35 kilobars. *Earth and Planetary Science Letters*, *25*(1), 44–48.
496 https://doi.org/10.1016/0012-821X(75)90208-3
497 Ichiki, M., Sumitomo, N., & Kagiyama, T. (2000). Resistivity structure of high-angle
498 subduction zone in the southern Kyushu district, southwestern Japan. *Earth, Planets and*
499 *Space*, *52*(8), 539–548. https://doi.org/10.5636/eps.52.539
500 Ito, E., Harris, D. M., & Anderson, A. T. (1983). Alteration of oceanic crust and geologic
501 cycling of chlorine and water. *Geochimica et Cosmochimica Acta*, *47*(9), 1613–1624.
502 https://doi.org/10.1016/0016-7037(83)90188-6
503 Jackson, M. G., Koga, K., Price, A. A., Konter, J. G., Koppers, A. A. P., Finlayson, V. ., et al.
504 (2015). Deeply dredged submarine HIMU glasses from the Tuvalu Islands, Polynesia:
505 Implications for volatile budgets of recycled oceanic crust. *Geochemistry, Geophysics,*
506 *Geosystems*, *16*, 3210–3234. https://doi.org/10.1002/2015GC005966
507 Jödicke, H., Jording, A., Ferrari, L., Arzate, J., Mezger, K., & Rüpke, L. (2006). Fluid release
508 from the subducted Cocos plate and partial melting of the crust deduced from
509 magnetotelluric studies in southern Mexico: Implications for the generation of volcanism
510 and subduction dynamics. *Journal of Geophysical Research: Solid Earth*, *111*(8), 1–22.
511 https://doi.org/10.1029/2005JB003739
512 Kawamoto, T., Hertwig, A., Schertl, H. P., & Maresch, W. V. (2018). Fluid inclusions in
513 jadeitite and jadeite-rich rock from serpentinite mélanges in northern Hispaniola:
514 Trapped ambient fluids in a cold subduction channel. *Lithos*, *308–309*, 227–241.
515 https://doi.org/10.1016/j.lithos.2018.02.024
516 Kendrick, M. A., Scambelluri, M., Honda, M., & Phillips, D. (2011). High abundances of

noble gas and chlorine delivered to the mantle by serpentinite subduction. *Nature Geoscience*, *4*(11), 807–812. https://doi.org/10.1038/ngeo1270

Kendrick, M. A., Jackson, M. G., Hauri, E. H., & Phillips, D. (2015). The halogen (F, Cl, Br, I) and H2O systematics of Samoan lavas: Assimilated-seawater, EM2 and high-3He/4He components. *Earth and Planetary Science Letters*, *410*, 197–209. https://doi.org/10.1016/j.epsl.2014.11.026

Kessel, R., Schmidt, M. W., Ulmer, P., & Pettke, T. (2005). Trace element signature of subduction-zone fluids, melts and supercritical liquids at 120-180 km depth. *Nature*, *437*(7059), 724–727. https://doi.org/10.1038/nature03971

Kovalenko, V. I., Naumov, V. B., Girnis, A. V., Dorofeeva, V. A., & Yarmolyuk, V. V. (2006). Composition and chemical structure of oceanic mantle plumes. *Petrology*, *14*(5), 452–476. https://doi.org/10.1134/S0869591106050031

Lee, S. K., & Stebbins, J. F. (2006). Disorder and the extent of polymerization in calcium silicate and aluminosilicate glasses: O-17 NMR results and quantum chemical molecular orbital calculations. *Geochimica et Cosmochimica Acta*, *70*(16), 4275–4286. https://doi.org/10.1016/j.gca.2006.06.1550

Locock, A. J. (2014). An Excel spreadsheet to classify chemical analyses of amphiboles following the IMA 2012 recommendations. *Computers and Geosciences*, *62*, 1–11. https://doi.org/10.1016/j.cageo.2013.09.011

Mandler, B. E., & Grove, T. L. (2016). Controls on the stability and composition of amphibole in the Earth's mantle. *Contributions to Mineralogy and Petrology*, *171*(8–9), 1–20. https://doi.org/10.1007/s00410-016-1281-5

Manthilake, G, Bolfan-Casanova, N., Novella, D., Mookherjee, M., & Andrault, D. (2016). Dehydration of chlorite explains anomalously high electrical conductivity in the mantle wedges. *Science Advances*, *2*(5). https://doi.org/10.1126/sciadv.1501631

542 Manthilake, G., Mookherjee, M., & Miyajima, N. (2021a). Insights on the deep carbon cycle
543 from the electrical conductivity of carbon-bearing aqueous fluids. *Scientific Reports*.
544 https://doi.org/10.1038/s41598-021-82174-8
545 Manthilake, G, Chantel, J., Guignot, N., & King, A. (2021b). The Anomalous Seismic
546 Behavior of Aqueous Fluids Released during Dehydration of Chlorite in Subduction
547 Zones. *Minerals*, *11*(70). https://doi.org/10.3390/min11010070
548 Manthilake, Geeth, Mookherjee, M., Bolfan-Casanova, N., & Andrault, D. (2015). Electrical
549 conductivity of lawsonite and dehydrating fluids at high pressures and temperatures.
550 *Geophysical Research Letters*, *42*(18), 7398–7405.
551 https://doi.org/10.1002/2015GL064804
552 Maroufi, S., Amini, S., Jahanshahi, S., & Ostrovski, O. (2016). Diffusion Coefficients and
553 Structural Parameters of Molten Slags. In *Advances in Molten Slags, Fluxes, and Salts*
554 (pp. 493–500). John Wiley & Sons, Ltd. https://doi.org/10.1002/9781119333197.ch52
555 Mathez, E. A., & Webster, J. D. (2005). Partitioning behavior of chlorine and fluorine in the
556 system apatite-silicate melt-fluid. *Geochimica et Cosmochimica Acta*, *69*(5), 1275–1286.
557 https://doi.org/10.1016/j.gca.2004.08.035
558 McGary, R. S., Evans, R. L., Wannamaker, P. E., Elsenbeck, J., & Rondenay, S. (2014).
559 Pathway from subducting slab to surface for melt and fluids beneath Mount Rainier.
560 *Nature*, *511*(7509), 338–340. https://doi.org/10.1038/nature13493
561 Mibe, K., Fujii, T., & Yasuda, A. (1999). Control of the location of the volcanic front in
562 island arcs by aqueous fluid connectivity in the mantle wedge. *Nature*, *401*(6750), 259–
563 262. https://doi.org/10.1038/45762
564 Mills, K. C. (1993). The Influence of Structure on the Physico-chemical Properties of Slags.
565 *Isij International*, *33*(1), 148–155. https://doi.org/10.2355/isijinternational.33.148
566 Mitchell, a. C., & Nellis, W. J. (1982). Equation of state and electrical conductivity of water

and ammonia shocked to the 100 GPa (1 Mbar) pressure range. *The Journal of Chemical Physics*, *76*(12), 6273–6281. https://doi.org/10.1063/1.443030

Ni, H., Keppler, H., & Behrens, H. (2011). Electrical conductivity of hydrous basaltic melts: Implications for partial melting in the upper mantle. *Contributions to Mineralogy and Petrology*, *162*(3), 637–650. https://doi.org/10.1007/s00410-011-0617-4

Reynard, B., Mibe, K., & de Moortèle, B. Van. (2011). Electrical conductivity of the serpentinised mantle and fluid flow in subduction zones. *Earth and Planetary Science Letters*, *307*(3–4), 387–394. https://doi.org/10.1016/j.epsl.2011.05.013

Roberge, M., Bureau, H., Bolfan-Casanova, N., Raepsaet, C., Surble, S., Khodja, H., et al. (2017). Chlorine in wadsleyite and ringwoodite: An experimental study. *Earth and Planetary Science Letters*, *467*, 99–107. https://doi.org/10.1016/j.epsl.2017.03.025

Rose-Koga, E. F., Koga, K. T., Moreira, M., Vlastelic, I., Jackson, M. G., Whitehouse, M. J., et al. (2017). Geochemical systematics of Pb isotopes, fluorine, and sulfur in melt inclusions from São Miguel, Azores. *Chemical Geology*, *458*, 22–37. https://doi.org/10.1016/j.chemgeo.2017.03.024

Rose-Koga, E. F., Koga, K. T., Devidal, J. L., Shimizu, N., Voyer, M. Le, Dalou, C., & Döbeli, M. (2020). In-situ measurements of magmatic volatile elements, F, S, and Cl, by electron microprobe, secondary ion mass spectrometry, and heavy ion elastic recoil detection analysis. *American Mineralogist*, *105*(5), 616–626. https://doi.org/10.2138/am-2020-7221

Sakuma, H., & Ichiki, M. (2016). Electrical conductivity of NaCl-H2O fluid in the crust. *Journal of Geophysical Research B: Solid Earth*, *121*(2), 577–594. https://doi.org/10.1002/2015JB012219

Scambelluri, M., Müntener, O., Ottolini, L., Pettke, T. T., & Vannucci, R. (2004). The fate of B, Cl and Li in the subducted oceanic mantle and in the antigorite breakdown fluids.

592 *Earth and Planetary Science Letters*, *222*(1), 217–234.
593 https://doi.org/10.1016/j.epsl.2004.02.012
594 Schmidt, M. W., & Poli, S. (1998). Experimentally based water budgets for dehydrating slabs
595 and consequences for arc magma generation. *Earth and Planetary Science Letters*,
596 *163*(1–4), 361–379. https://doi.org/10.1016/S0012-821X(98)00142-3
597 Shen, K., Wang, D., & Liu, T. (2020). Electrical conductivity of tremolite under high
598 temperature and pressure: implications for the high-conductivity anomalies in the Earth
599 and Venus. *Contributions to Mineralogy and Petrology*, *175*(5), 1–12.
600 https://doi.org/10.1007/s00410-020-01688-y
601 Shimojuku, A., Yoshino, T., Yamazaki, D., & Okudaira, T. (2012). Electrical conductivity of
602 fluid-bearing quartzite under lower crustal conditions. *Physics of the Earth and*
603 *Planetary Interiors*, *198–199*, 1–8. https://doi.org/10.1016/j.pepi.2012.03.007
604 Shimojuku, A., Yoshino, T., & Yamazaki, D. (2014). Electrical conductivity of brine-bearing
605 quartzite at 1 GPa: implications for fluid content and salinity of the crust. *Earth, Planets*
606 *and Space*, *66*(1), 2. https://doi.org/10.1186/1880-5981-66-2
607 Sinmyo, R., & Keppler, H. (2017). Electrical conductivity of NaCl-bearing aqueous fluids to
608 600 °C and 1 GPa. *Contributions to Mineralogy and Petrology*, *172*(1), 1–12.
609 https://doi.org/10.1007/s00410-016-1323-z
610 Soustelle, V., Walte, N. P., Manthilake, M. A. G. M., & Frost, D. J. (2014). Melt migration
611 and melt-rock reactions in the deforming Earth's upper mantle: Experiments at high
612 pressure and temperature. *Geology*, *42*(1), 83–86. https://doi.org/10.1130/G34889.1
613 Soyer, W., & Unsworth, M. (2006). Deep electrical structure of the northern Cascadia (British
614 Columbia, Canada) subduction zone: Implications for the distribution of fluids. *Geology*,
615 *34*(1), 53–56. https://doi.org/10.1130/G21951.1
616 Straub, S. M., & Layne, G. D. (2003). Decoupling of fluids and fluid-mobile elements during

shallow subduction: Evidence from halogen-rich andesite melt inclusions from the Izu arc volcanic front. *Geochemistry, Geophysics, Geosystems*, *4*(7). https://doi.org/10.1029/2002GC000349

Wallace, P. J. (2005). Volatiles in subduction zone magmas: Concentrations and fluxes based on melt inclusion and volcanic gas data. *Journal of Volcanology and Geothermal Research*, *140*(1–3), 217–240. https://doi.org/10.1016/j.jvolgeores.2004.07.023

Wang, D., & Karato, S. ichrio. (2013). Electrical conductivity of talc aggregates at 0.5 GPa: Influence of dehydration. *Physics and Chemistry of Minerals*, *40*(1), 11–17. https://doi.org/10.1007/s00269-012-0541-9

Wang, D., Guo, Y., Yu, Y., & Karato, S. ichiro. (2012). Electrical conductivity of amphibole-bearing rocks: Influence of dehydration. *Contributions to Mineralogy and Petrology*, *164*(1), 17–25. https://doi.org/10.1007/s00410-012-0722-z

Wannamaker, P. E., Caldwell, T. G., Jiracek, G. R., Maris, V., Hill, G. J., Ogawa, Y., et al. (2009). Fluid and deformation regime of an advancing subduction system at Marlborough, New Zealand. *Nature*, *460*(7256), 733–736. https://doi.org/10.1038/nature08204

Webster, J. D., Tappen, C. M., & Mandeville, C. W. (2009). Partitioning behavior of chlorine and fluorine in the system apatite-melt-fluid. II: Felsic silicate systems at 200 MPa. *Geochimica et Cosmochimica Acta*, *73*(3), 559–581. https://doi.org/10.1016/j.gca.2008.10.034

Weidner, D. J., Li, L., Whitaker, M. L., & Triplett, R. (2018). Ultrasonic Acoustic Velocities During Partial Melting of a Mantle Peridotite KLB-1. *Journal of Geophysical Research: Solid Earth*, *123*(2), 1252–1261. https://doi.org/10.1002/2017JB014753

Worzewski, T., Jegen, M., Kopp, H., Brasse, H., & Taylor Castillo, W. (2011). Magnetotelluric image of the fluid cycle in the Costa Rican subduction zone. *Nature*

642 *Geoscience*, *4*(2), 108–111. https://doi.org/10.1038/ngeo1041
643 Wu, J., & Koga, K. T. (2013). Fluorine partitioning between hydrous minerals and aqueous
644 fluid at 1GPa and 770-947°C: A new constraint on slab flux. *Geochimica et*
645 *Cosmochimica Acta*, *119*, 77–92. https://doi.org/10.1016/j.gca.2013.05.025
646 Wu, J., & Koga, K. T. (2018). Direct analyses of fluorine in aqueous fluids extracted from 1-
647 GPa experiments. *Chemical Geology*, *502*, 44–54.
648 https://doi.org/10.1016/j.chemgeo.2018.10.011
649 Wyllie, P. J., & Wolf, M. B. (1993). Amphibolite dehydration-melting: Sorting out the
650 solidus. *Geological Society Special Publication*, *76*(76), 405–416.
651 https://doi.org/10.1144/GSL.SP.1993.076.01.20
652 Yoshino, T., & Jaseem, V. (2018). Fluorine solubility in bridgmanite: A potential fluorine
653 reservoir in the Earth's mantle. *Earth and Planetary Science Letters*, *504*, 106–114.
654 https://doi.org/10.1016/j.epsl.2018.10.009
655 Yoshino, T., Mibe, K., Yasuda, A., & Fujii, T. (2002). Wetting properties of anorthite
656 aggregates: Implications for fluid connectivity in continental lower crust. *Journal of*
657 *Geophysical Research: Solid Earth*, *107*(B1), ECV 10-1-ECV 10-8.
658 https://doi.org/10.1029/2001jb000440
659 Yoshino, T., Yamazaki, D., & Mibe, K. (2009). Well-wetted olivine grain boundaries in
660 partially molten peridotite in the asthenosphere. *Earth and Planetary Science Letters*,
661 *283*(1–4), 167–173. https://doi.org/10.1016/j.epsl.2009.04.007
662 Zhang, B., Yoshino, T., Yamazaki, D., Manthilake, G., & Katsura, T. (2014). Electrical
663 conductivity anisotropy in partially molten peridotite under shear deformation. *Earth and*
664 *Planetary Science Letters*, *405*, 98–109. https://doi.org/10.1016/j.epsl.2014.08.018
665
666

667 **Figure captions**

668 **Figure 1. (a)** Schematic cross-section of the high-pressure cell-assembly used for the electrical
669 conductivity measurements. The backscattered electron (BSE) images of (b) Fe kaersutite, (c)
670 actinolite, (d) hastingsite, (e) tremolite. The BSE images were acquired after the electrical
671 conductivity measurements.

672

673 **Figure 2.** Cole-cole plot of actinolite sample with increasing temperature. (a) At temperatures
674 below dehydration (673 K), conduction is through minerals in solid-state. The conductivity of
675 the solid mineral grains could be modeled with an R-CPE circuit, with a phase angle of 15.5
676 degrees. (b) At 841 K, the impedance spectrum shows the development of an inductive loop in
677 response to the onset of dehydration. The equivalent circuit can be represented as an R-CPE
678 with inductive component L. The induction at low frequencies may due to the adsorption of
679 ionic species in the electrode surface or erosion of electrodes due to fluid phases. (c) Further
680 increase in temperature to 1258 K results in a sudden decrease in sample resistance. The
681 persisting induction in impedance spectra indicates a possible reaction of melt with Ni
682 electrodes.

683

684 **Figure 3.** A plot of electrical conductivity of amphibole as a function of reciprocal temperature.
685 The symbols, blue, black, and red indicate solid, fluid, and melt, respectively. Activation
686 enthalpies below dehydrating temperatures are indicated in eV, next to individual fits. The
687 vertical lines indicate possible dehydration / melting temperatures for each mineral phase. The
688 uncertainties in electrical conductivity result from the estimations of temperature, pressure,
689 sample dimensions and data fitting errors and are estimated to be less than 5 %. Error bars are
690 smaller than the size of the markers.

691

**Figure 4.** Electron back-scattered image and the corresponding energy-dispersive X-ray spectroscopy (EDS) chemical map amphibole sample after the electrical conductivity measurements. (a) BSE image of exp. 554 Fe-Kaersutite breakdown. (b) Result of phase identification. P1 (red) is the remains of the initial Fe-Kaersutite, P2 (green) is garnet, P3 (blue) is the secondary garnet, P4 (light blue) is olivine but it appears to be metastable intermediate composition, P5 (purple) is porosity. (c) BSE image of exp. 555 actinolite breakdown showing porous texture with a bi-phase assembly. (d) Result of phase identification analysis. P1 (red) is cpx, P2 (green) is opx, and P3 (blue) corresponds to a high porosity zone with a high Cl signal. (e) BSE image of exp. 567 hastingsite breakdown. This starting material had some inclusions in the picked crystal, resulting in a larger number of phases in the charge. (f) Result of phase identification. P1 (red) indicates amphiboles, but it was not possible to distinguish the initial and secondary amphibole, as their compositional change was subtle. P2 (green) is opx. P3 (blue) is melt. P4 (light blue) is magnetite. P5 (purple) is ilmenite. P6 (yellow) is calcite. P7 (orange) is isolated tiny dots, which are the noise of EDS image. (g) BSE image of exp. 576 tremolite breakdown showing a porous texture. (h) Result of phase identification is shown in colors. P1 (red) remains of the initial tremolite, P2 (green) is the secondary amphibolite, fluoro-edenite. P3 (blue) is opx in needle form. Note opx and cpx are included in poikilitic fluoro-edenite. P4 (light blue) is melt. P5 (purple) corresponds to the high porosity zone.

**Figure 5.** A compilation of electrical conductivity data of hydrous minerals, dehydrating fluids, and hydrous melt. The vertical lines represent arbitrary boundaries defined based on talc (tlc) (Guo et al., 2011; Wang & Karato, 2013), serpentine (serp) (Reynard et al., 2011), chlorite (chl) (Manthilake et al., 2016) and amp (this study) and there dehydrating products. The electrical conductivity of saline fluids, basaltic melt (Gailler et al., 2019; Ni et al., 2011) and magnetite precipitates (Manthilake et al., 2016) are shown for comparison.

**Figure 6.** The energy-dispersive X-ray spectroscopy (EDS) chemical map showing the F concentrations of tremolite samples after dehydration. The F is mostly incorporated into the secondary fluoro-edenite (Ed) (green shades). The hydrous melt is shown in blue.

**Figure 7.** A plot of the logarithm of electrical conductivity of melt as a function of the $Na_2O$, FeO, and CaO wt % in the melt. Solid lines represent linear fits through data points with $(1.0927 \pm 2.7093) + (1.171 \pm 0.7342)x$ for $Na_2O$, $(1.9912 \pm 1.6585) + (0.503331 \pm 0.23433)x$ for FeO, and $(5.2806 \pm 5.7038) - (0.11349 \pm 0.52924)x$ for CaO. The electrical conductivities of melt were taken at the highest temperature of each experiment.

**Figure 8.** Electrical conductivity of a variety of fluid and melt compared with the range of values reported for subduction zones. The electrical conductivity presented in the figure are from the Cascadia subduction system (Evans et al., 2014; Soyer & Unsworth, 2006), Cocos subduction system in Sothern Mexico (Jödicke et al., 2006), Marlborough, New Zealand (Wannamaker et al., 2009) Northwestern Costa Rica (Brasse et al., 2009; Worzewski et al., 2011), Bolivia-Altiplano (Brasse et al., 2002), Bolivian Orocline (Brasse & Eydam, 2008) and Southern Kyushu (Ichiki et al., 2000).

**List of tables.**

**Table 1.** Pressures and temperatures explored in this study and the resulting phases including secondary mineral phases, fluids, and melts.

741 **Table 2.** Chemistry of the primary amphiboles and the secondary mineral phases produced after

742 dehydration and dehydration melting.

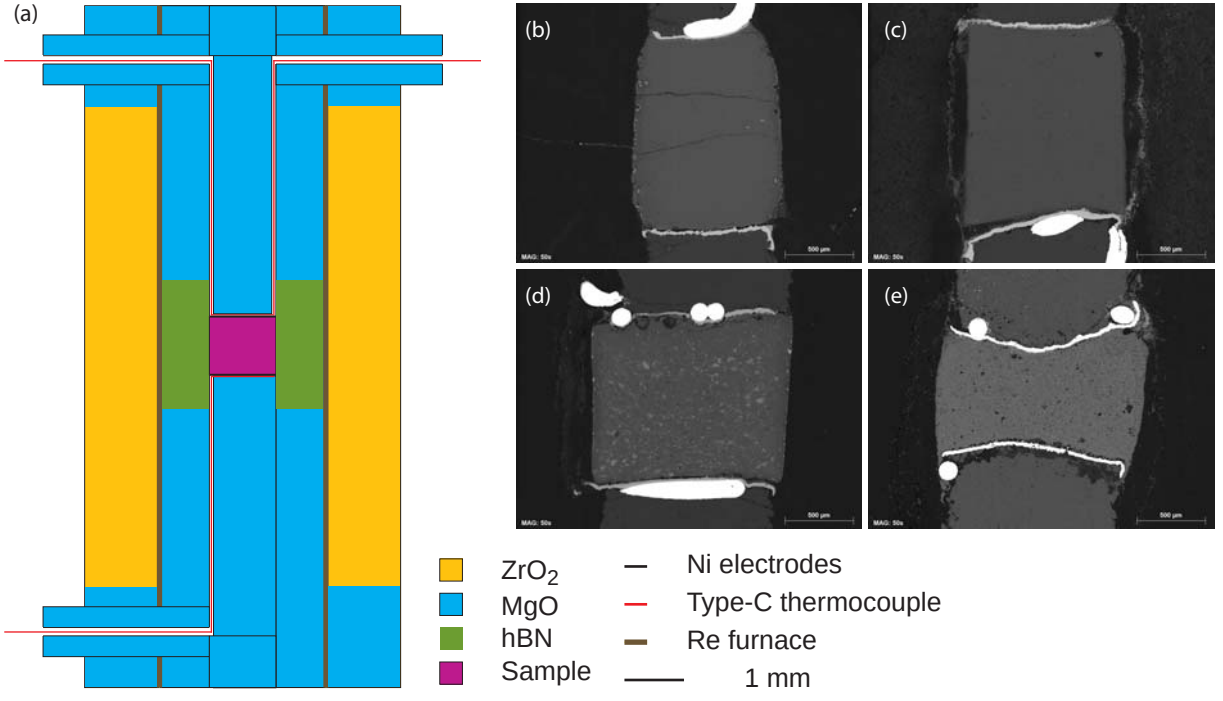
(a)
(b)
(c)
(d)
(e)
$ZrO_2$
MgO
hBN
Sample
Ni electrodes
Type-C thermocouple
Re furnace
1 mm

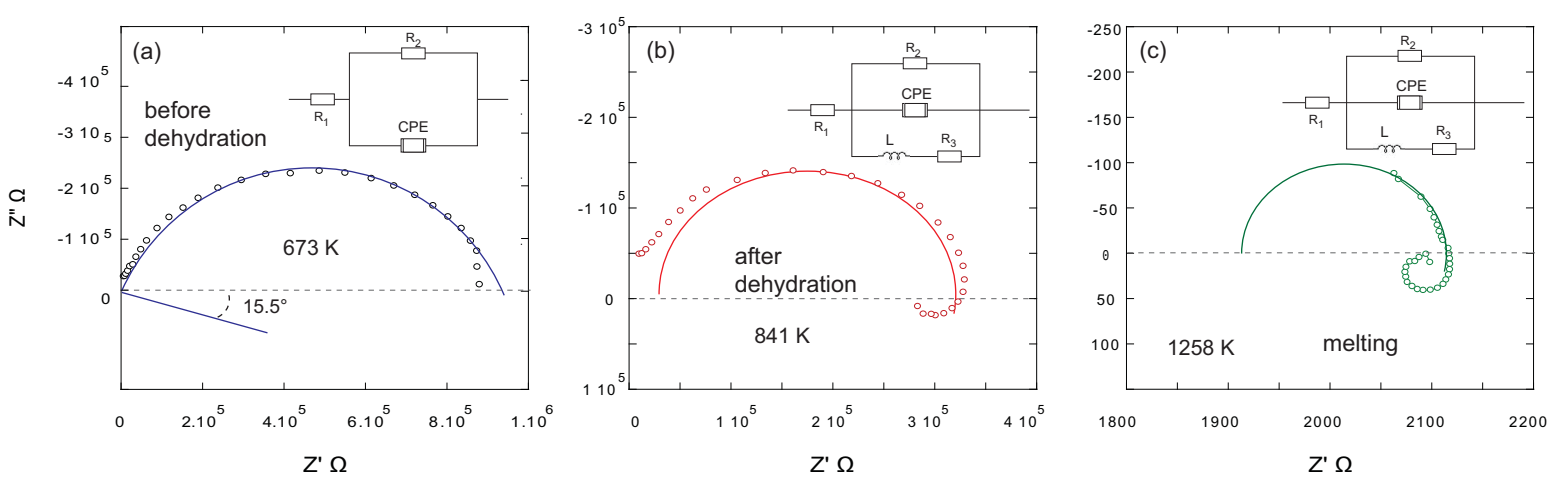
(a)
before dehydration
673 K
15.5°
R2
R1
CPE
-4 10^5
-3 10^5
-2 10^5
-1 10^5
0
0
2.10^5
4.10^5
6.10^5
8.10^5
1.10^6
Z'' Ω
Z' Ω
(b)
after dehydration
841 K
R2
CPE
R1
L
R3
-3 10^5
-2 10^5
-1 10^5
0
1 10^5
0
1 10^5
2 10^5
3 10^5
4 10^5
Z' Ω
(c)
1258 K
melting
R2
CPE
R1
L
R3
-250
-200
-150
-100
-50
0
50
100
1800
1900
2000
2100
2200
Z' Ω

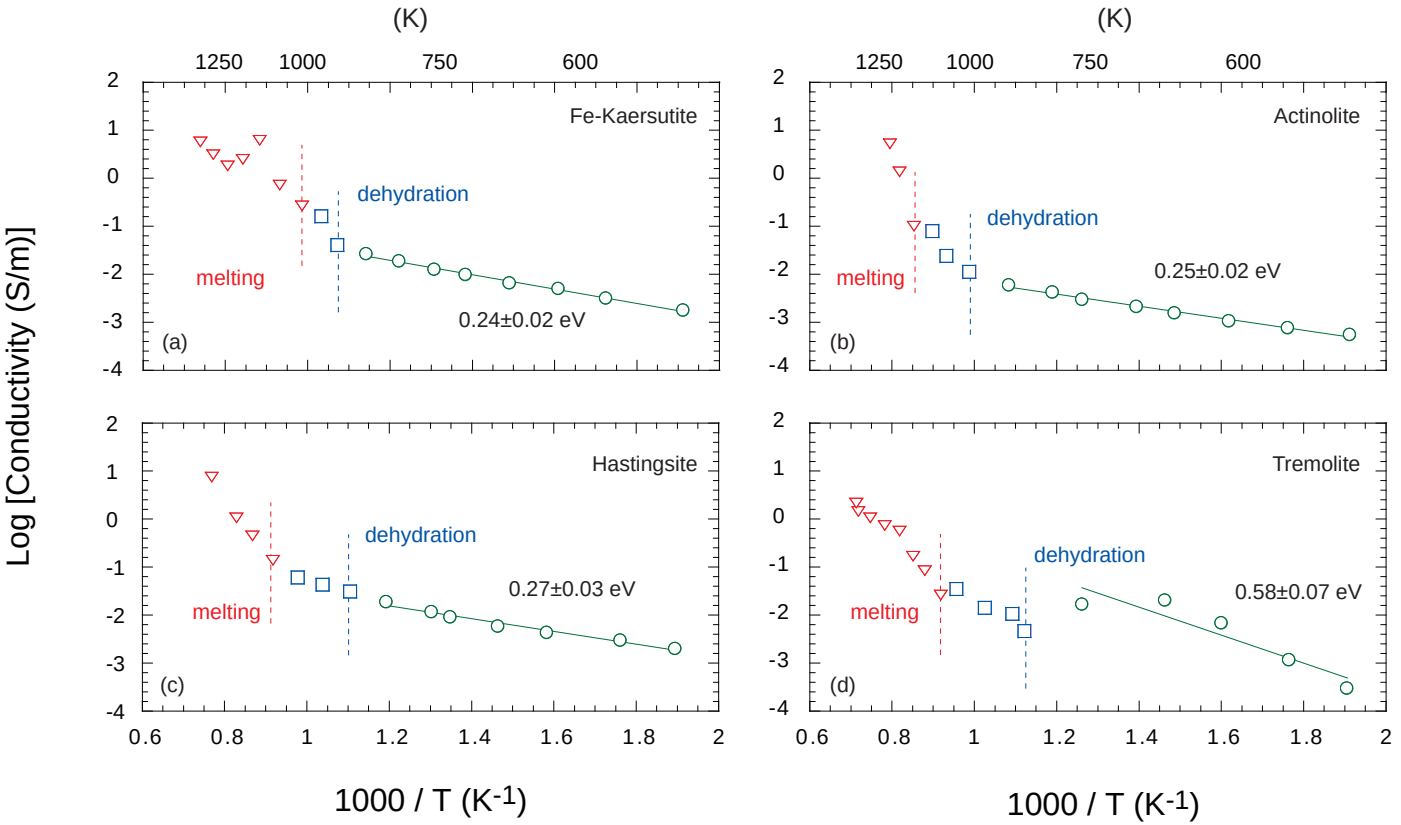
(K)
1250
1000
750
600
Fe-Kaersutite
dehydration
melting
0.24±0.02 eV
(a)
Actinolite
dehydration
melting
0.25±0.02 eV
(b)
Hastingsite
dehydration
melting
0.27±0.03 eV
(c)
Tremolite
dehydration
melting
0.58±0.07 eV
(d)
Log [Conductivity (S/m)]
1000 / T (K-1)

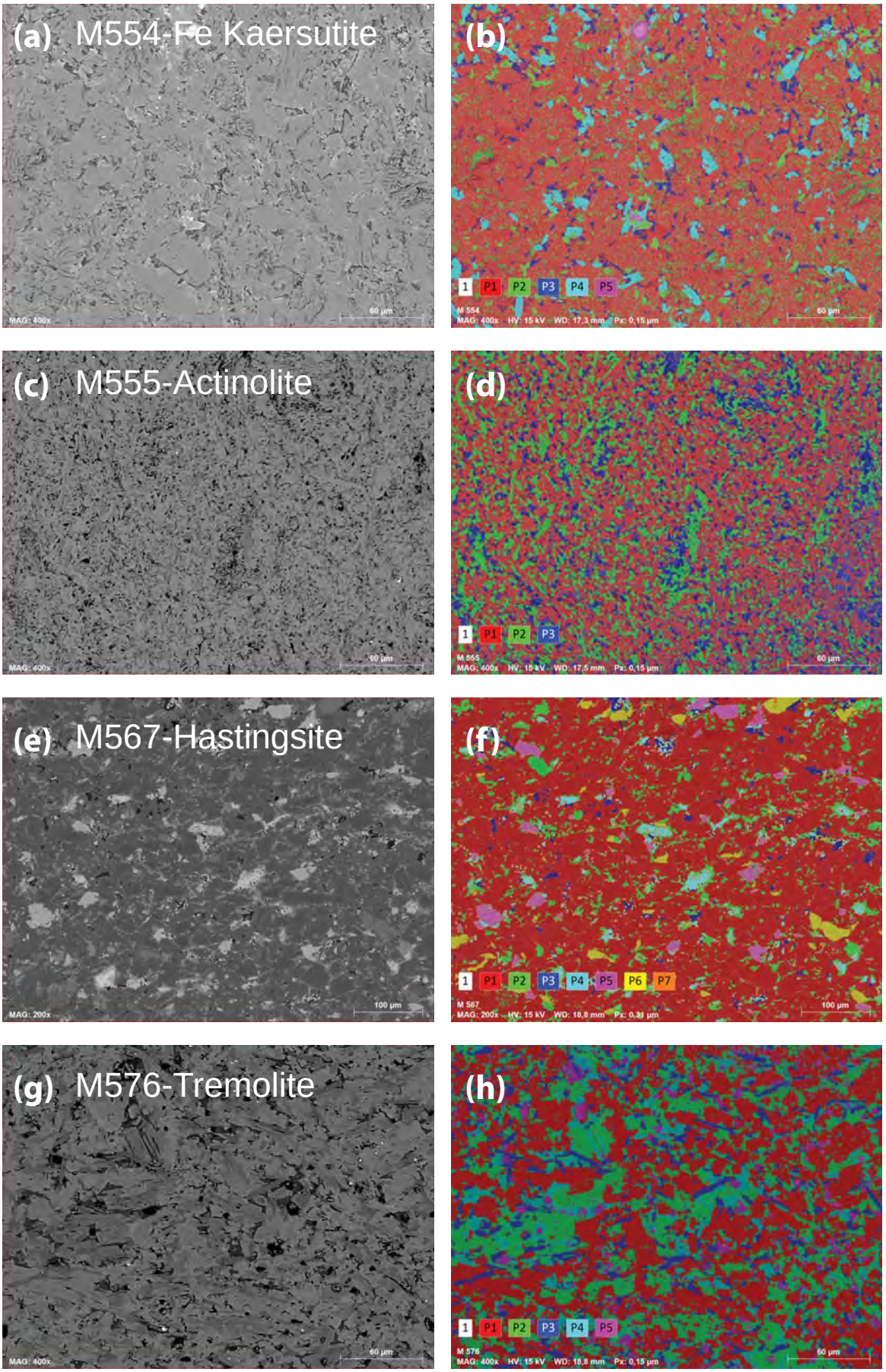
(a) M554-Fe Kaersutite
(b)
1 P1 P2 P3 P4 P5
(c) M555-Actinolite
(d)
1 P1 P2 P3
(e) M567-Hastingsite
(f)
1 P1 P2 P3 P4 P5 P6 P7
(g) M576-Tremolite
(h)
1 P1 P2 P3 P4 P5

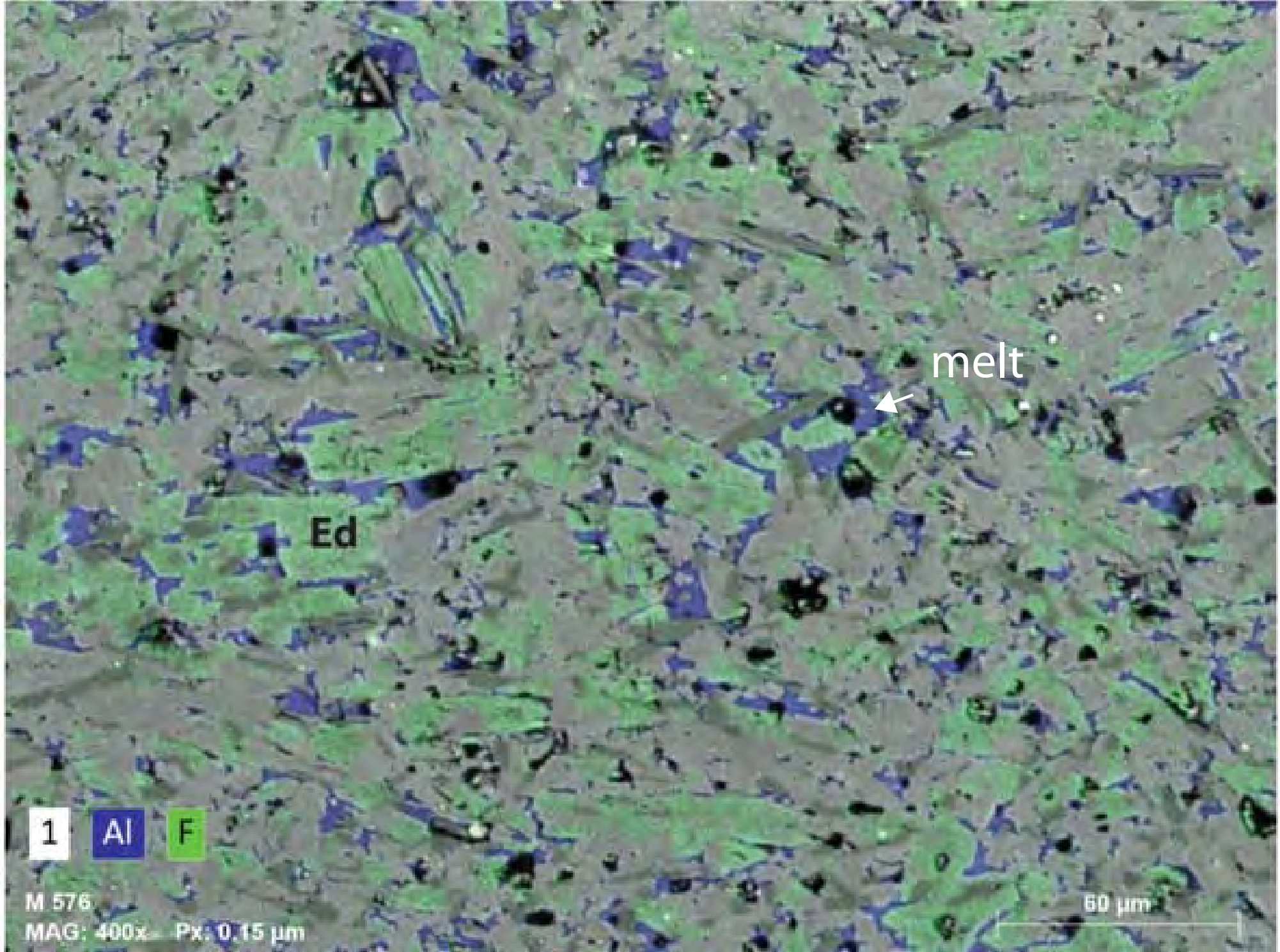
melt
Ed
1
Al
F
M 576
MAG: 400x Px: 0.15 µm
60 µm

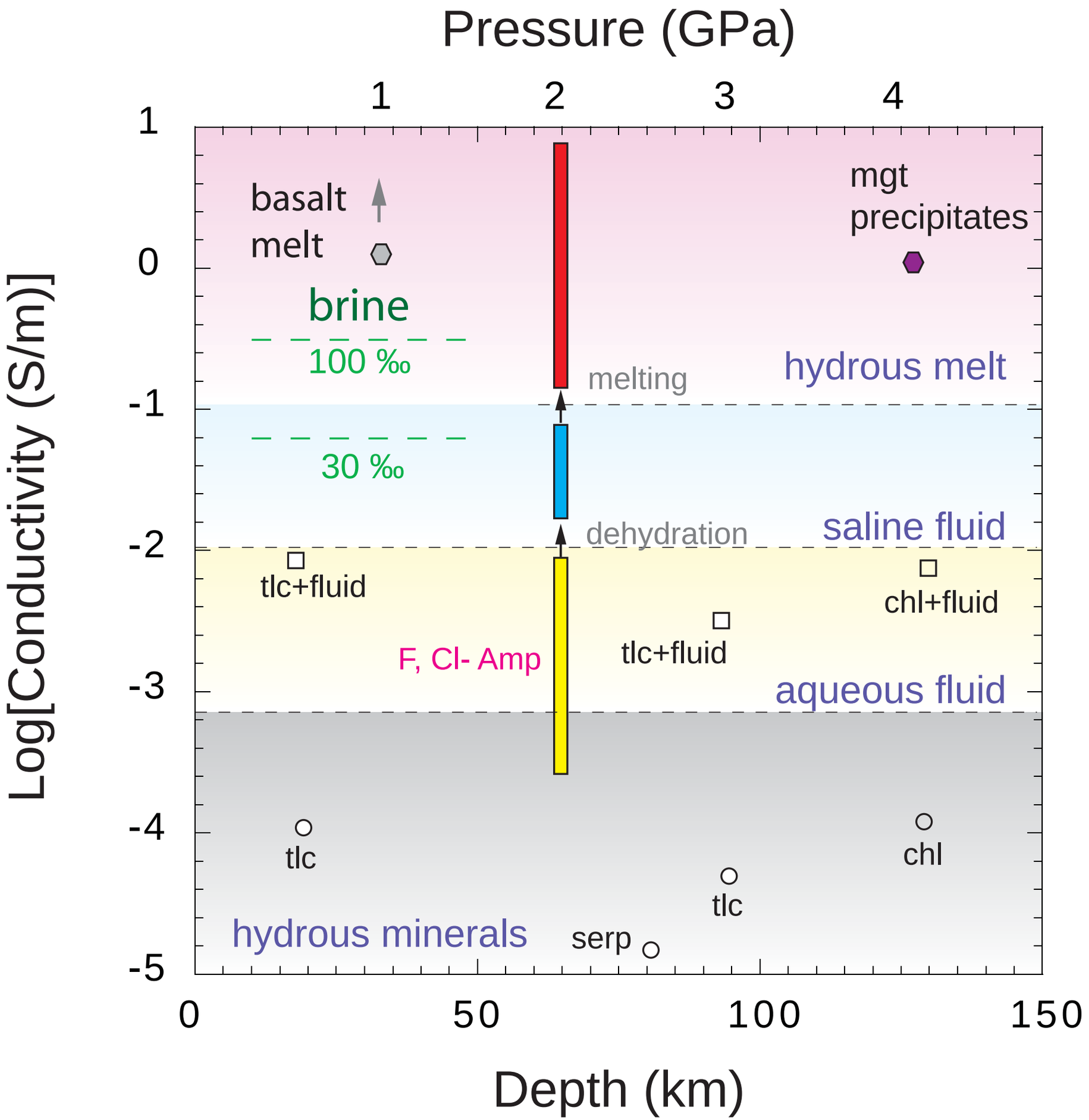
Pressure (GPa)
1
2
3
4
Log[Conductivity (S/m)]
1
0
-1
-2
-3
-4
-5
basalt
melt
brine
100 ‰
30 ‰
mgt
precipitates
hydrous melt
melting
saline fluid
dehydration
aqueous fluid
F, Cl- Amp
tlc+fluid
tlc+fluid
chl+fluid
tlc
tlc
chl
serp
hydrous minerals
0
50
100
150
Depth (km)

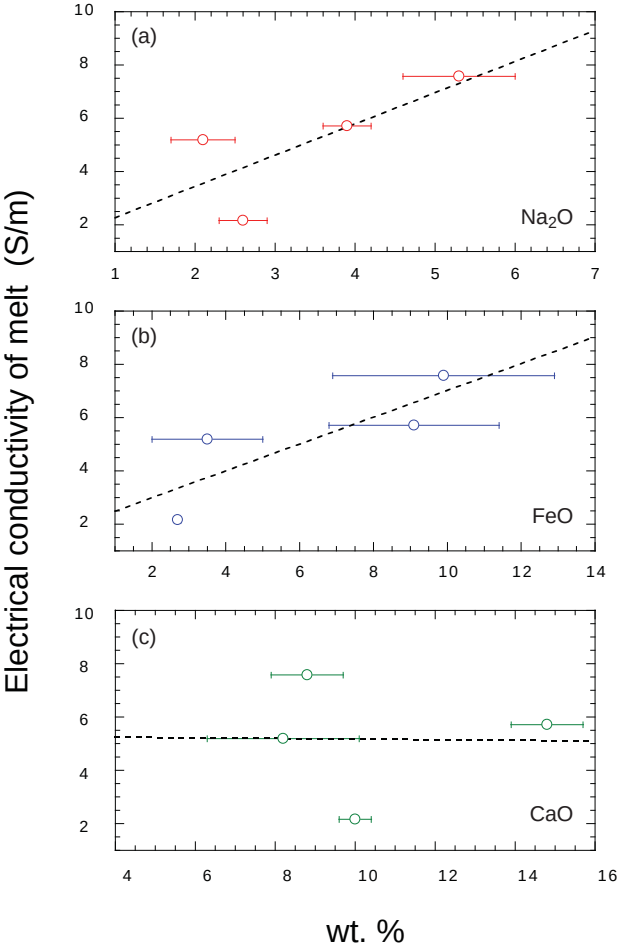
Electrical conductivity of melt (S/m)
(a)
Na2O
(b)
FeO
(c)
CaO
wt. %

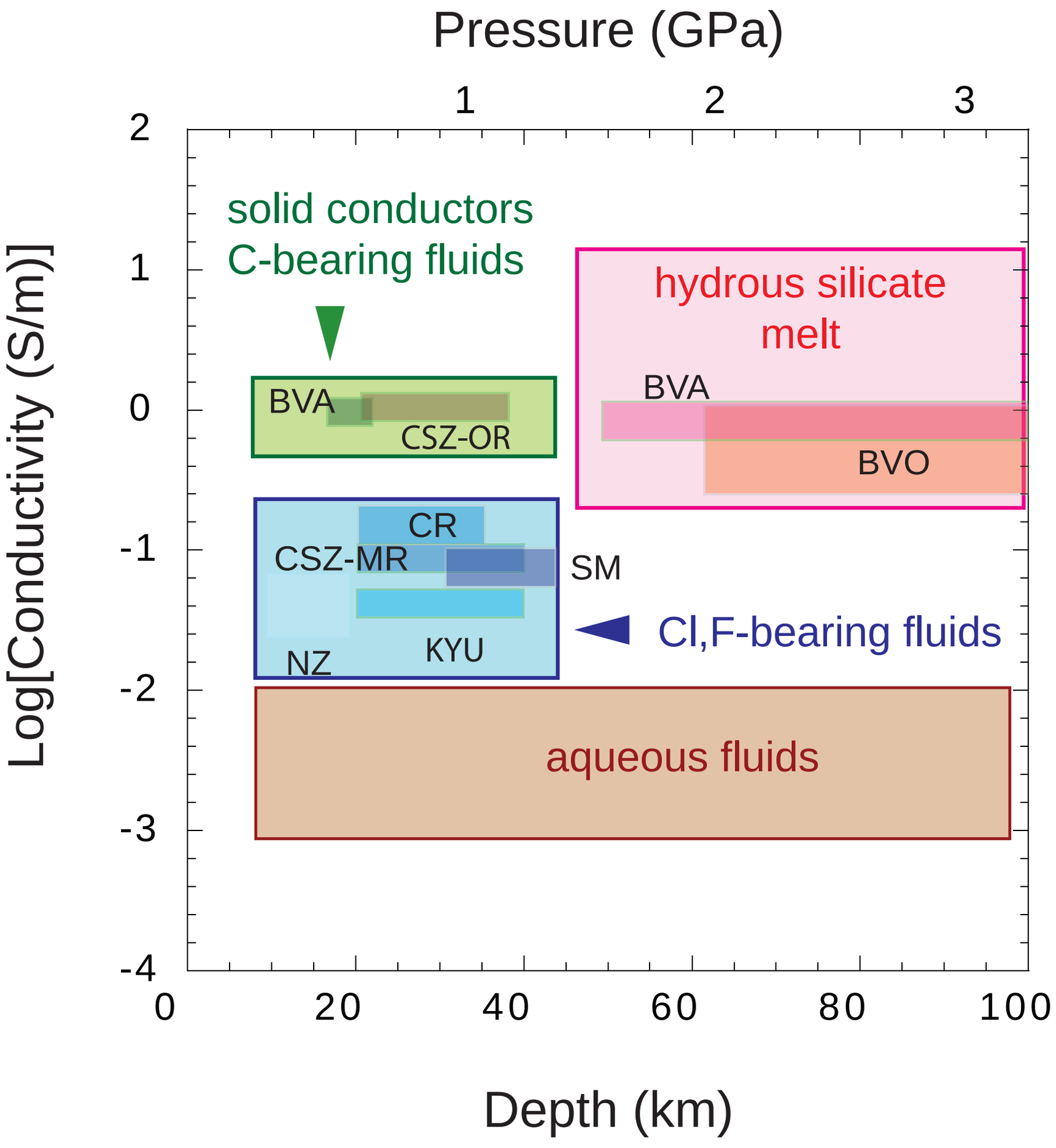
Pressure (GPa)
1
2
3
2
1
0
-1
-2
-3
-4
Log[Conductivity (S/m)]
solid conductors
C-bearing fluids
BVA
CSZ-OR
hydrous silicate
melt
BVA
BVO
CR
CSZ-MR
SM
Cl,F-bearing fluids
KYU
NZ
aqueous fluids
0
20
40
60
80
100
Depth (km)

**Table 1. Experimental conditions**

| Exp. | P (GPa) | $T_1$ (K) | $T_2$ (K) | Reaction | % rest |
|---|---|---|---|---|---|
| M554 | 1.5 | 933 | 1392 | Fe Kaersutite = 0.50 Gt + 0.18 Ol + 0.32 Liq (melt) | 62 |
| M555 | 1.5 | 923 | 1258 | Actinolite = 0.58 Cpx + 0.14 Opx + 0.28 Liq (melt) | 0 |
| M567 | 1.5 | 1091 | 1301 | Hastigsite = 0.58 Kearsutite + 0.01 Opx + 0.42 Liq (melt) | 76 |
| M576 | 1.5 | 915 | 1402 | Tremolite = 0.70 Cpx + 0.15 Opx + 0.17 Liq (Low T)<br>Tremolite = 0.35 F edenite + 0.65 Liq (High T) | 47 |

Exp., experiment run number. P, the pressure condition of the experiment. T1 and T2, temperature conditions corresponding to the interval of the reaction, identified on the bases of the activation enthalpy. Reaction, mineral assemblages are expressed as a product stoichiometry determined by mass-balance calculations with the procedure described in Wu and Koga (2013). Phase compositions are given in Table 2. The starting amphibole is taken as unity. % rest, the fraction of initial amphibole remained in the experiment at the end of the experiment, determined by SEM image analysis.

Table 2. Composition of mineral phases after dehydration and melting

| | Fe-Krs=Gt+Ol+liq | | | | Act=Cpx+Opx+liq | | | | Hst=Krs+En+Liq | | | | Tr=F-Ed+liq | | |
|---|---|---|---|---|---|---|---|---|---|---|---|---|---|---|---|
| **Phase** | Krs* | Gt | Ol | Melt | Act* | Cpx | Opx | Melt | Hst* | Krs | En | Melt | Tr* | F-Ed | melt |
| **$SiO_2$** | 39.0(7) | 40.2(14) | 34.9(17) | 42.2(31) | 57.1(8) | 55.2(2) | 57.1(5) | 61.0(28) | 43.1(13) | 38.4(8) | 58.9(2) | 48.3(29) | 56.9(8) | 56.00(5) | 55.2(4) |
| **$TiO_2$** | 5.4(2) | 7.6(2) | 3.37(6) | 3.5(7) | 0.03(4) | 0.04(1) | 0.01(2) | 0.03(14) | 3.8(6) | 5.1(5) | 0.06(1) | 2.2(17) | 0.08(4) | 0.17(3) | 0.23(5) |
| **$Al_2O_3$** | 13.9(3) | 15.1(13) | 7.4(9) | 16.6(21) | 1.18(9) | 1.4(4) | 0.9(4) | 0.8(8) | 9.7(7) | 14.8(5) | 0.31(3) | 2.9(19) | 1.3(1) | 1.28(9) | 1.7(2) |
| **$Cr_2O_3$** | 0.02(2) | 0.02(1) | 0.00 | 0.02(7) | 0.00 | 0.00 | 0.00 | 0.00 | 0.02(2) | 0.04(3) | 0.003(4) | 0.00 | 0.00 | 0.00 | 0.00 |
| **FeO** | 11.2(5) | 9.8(9) | 20.4(19) | 9.1(23) | 4.9(4) | 5.1(4) | 7.3(3) | 3.5(15) | 13.7(12) | 16.4(8) | 3.84(2) | 9.9(30) | 2.9(3) | 2.79(5) | 2.6(1) |
| **MnO** | 0.10(3) | 0.11(0) | 0.15(5) | 0.08(9) | 0.3(2) | 0.40(3) | 0.42(4) | 0.00 | 0.23(9) | 0.26(5) | 0.06(1) | 0.2(2) | 0.1(1) | 0.08(2) | 0.07(3) |
| **MgO** | 11.9(4) | 12.3(9) | 24.4(6) | 5.4(19) | 21.1(3) | 21.1(7) | 30.6(3) | 16.3(19) | 13.1(5) | 8.5(5) | 33.9(7) | 18.5(14) | 22.4(3) | 24.6(9) | 23.2(5) |
| **CaO** | 11.6 (2) | 12.0(4) | 6.3(8) | 14.8(9) | 11.6(2) | 15.5(8) | 2.5(4) | 8.2(19) | 9.9(4) | 10.8(2) | 2.7(1) | 8.8(9) | 12.7(2) | 9.6(11) | 10.0(4) |
| **$Na_2O$** | 2.16(8) | 1.6(1) | 0.71(0) | 3.9(3) | 0.8(1) | 0.28(7) | 0.05(2) | 2.1(4) | 3.9(3) | 2.9(2) | 0.08(5) | 5.3(7) | 1.0(1) | 1.94(9) | 2.6(3) |
| **$K_2O$** | 1.65(9) | 1.9(1) | 0.27(4) | 2.1(4) | 0.05(2) | 0.01(1) | 0.01(0) | 0.17(9) | 0.16(2) | 0.16(2) | 0.06(8) | 0.16(7) | 0.38(4) | 0.75(4) | 1.1(1) |
| **F** | 0.17(2) | 0.34(8) | 0.00 | 0.00 | 0.02(0) | 0.00 | 0.00 | 0.09(11) | 0.21(8) | 0.22(1) | 0.48(10) | 0.18(20) | 0.79(2) | 3.3(4) | 0.1(1) |
| **Cl** | 0.022(2) | 0.03(1) | 0.00 | 0.02(4) | 0.004(1) | 0.00 | 0.00 | 0.01(11) | 0.03(3) | 0.006(5) | 1.02(5) | 0.03(7) | 0.012(2) | 0.03(4) | 0.01(1) |
| **H2O+** | 0.71(5) | 0.00 | 0.00 | 2.3(3) | 2.16(5) | 0.00 | 0.00 | 7.7(2) | 1.92(4) | 0.72(21) | 0.00 | 3.6(3) | 1.63(4) | 0.01(10) | 2.56(5) |
| **Total** | **97.87** | **101.01** | **97.61** | **100.00** | **99.24** | **99.01** | **98.82** | **100.00** | **99.88** | **98.41** | **101.48** | **100.00** | **100.18** | **100.58** | **99.17** |

Measurements by an electron microprobe are reported here. Values in parentheses represent one standard deviation on the averages in terms of the smallest units cited. For example, 39.0(7) should read as 39.0 +/- 0.7. H2O+: the values are determined by the stoichiometric balance of amphibole composition following the procedure of Locock (2014). Met compositions are determined by a modified mass-balance procedure (Wu and Koga 2013). *starting amphiboles remaining in the sample after the dehydration-melting